

Surface states and finite size effects in triple-fold semimetals

A.Yu. Prykhodko,¹ E.V. Gorbar,^{1,2,*} and P.O. Sukhachov^{3,4,†}

¹*Faculty of Physics, Kyiv National Taras Shevchenko University, 64/13 Volodymyrska st., 01601 Kyiv, Ukraine*

²*Bogolyubov Institute for Theoretical Physics, 14-b Metrolohichna st., 03143 Kyiv, Ukraine*

³*Department of Physics and Astronomy, University of Missouri, Columbia, Missouri, 65211, USA*

⁴*MU Materials Science & Engineering Institute, University of Missouri, Columbia, Missouri, 65211, USA*

(Dated: June 23, 2025)

Triple-fold or pseudospin-1 semimetals belong to a class of multi-fold materials in which linearly dispersive bands and flat bands intersect at the same point, forming triple-fold crossing points. We conduct an analytical investigation of topologically protected Fermi arc surface states and finite-size effects in three-dimensional (3D) triple-fold and doubly degenerate triple-fold semimetals in continuum low-energy models. Higher topological charge of the triple-fold crossing points leads to two Fermi arcs connecting the nodes. For a single triple-fold crossing point, we found that no term in the Hamiltonian with momentum-independent elements can open a gap, prompting us to consider a doubly-degenerate triple-fold fermion, where the gap can be opened by mixing the degenerate copies. Thin films of triple-fold semimetals allow for mixing between the surface and bulk states in addition to the discretization of energy levels of the latter.

I. INTRODUCTION

The discovery of Dirac [1–6] and Weyl [7–13] semimetals, featuring band-crossing points or nodes with linear dispersion relation and quasiparticles described by the relativistic-like Dirac and Weyl equations, has opened up a new research field known as topological semimetals [14–20]. While each Dirac point is composed of two Weyl nodes of opposite topological charge in Dirac semimetals, Weyl nodes are separated in momentum space in Weyl semimetals. Being a condensed matter analog of Weyl fermions, Weyl quasiparticles allow one to realize several effects previously predicted in the high-energy physics setting. The celebrated chiral anomaly [21, 22] is an illustrative example that is manifested in, e.g., negative magnetoresistivity [23–29].

In addition to pseudospin-1/2 Weyl quasiparticles, spatial symmetry in crystals allows for the existence of other types of fermions with higher pseudospin and dispersion laws that have no analogs in particle physics [30]. In particular, the energy spectrum of the multi-fold semimetals contains nodes where several bands intersect at the same point. For example, triple-point or pseudospin-1 topological metals contain nodes where Dirac cones are intersected by an additional flat (weakly dispersive) band [31].

Historically, the appearance of flat bands in two-dimensional (2D) systems was predicted a few decades ago in kagomé [32], dice or $\alpha - \mathcal{T}_3$ [33, 34], and Lieb [35] lattices. The macroscopic degeneracy of electronic flat band states plays an important role in the thermodynamic, electronic, topological, and optical properties of the corresponding systems, see Refs. [36–40]. In three dimensions (3D), it was experimentally shown that CoSi [41–44], RhSi [43], and AlPt [45] are multi-fold

semimetals which realize triple-, four-, and six-fold nodes. Being compatible with Si technology, CoSi attracted significant attention as a material that could enhance the transport properties of electronic devices [46, 47].

Like Weyl semimetals, pseudospin-1 semimetals are topological, whose nontrivial topology is manifested in the presence of topologically protected surface states. In Weyl semimetals, such states are known as Fermi arcs [48, 49]. The Fermi arcs connect the projections of the Weyl nodes of opposite topological charges onto the surface Brillouin zone. In multi-fold semimetals, there are also topological Fermi arc surface states. The Fermi arcs are long and chiral [43], leading to enhanced optical response [50].

Until now, the properties of the Fermi arc surface states in multi-fold semimetals were studied mostly via numerical methods using tight-binding models [51, 52]. In this work, we develop an analytical low-energy continuum model for the Fermi arc surface states in slabs of triple-fold semimetals, where we focus on the interplay of flat and dispersive bands. We show that, in agreement with the topological charge of dispersive bands, there are two Fermi arcs per triple-fold node: one connects the nodes and the other radiates away. While the latter is reminiscent of the long arc spanning the whole Brillouin zone observed in CoSi and RhSi [41–44], its behavior away from the nodes requires a model that is valid beyond the vicinity of crossing points, ideally in the whole Brillouin zone. In thin films, finite size effects make the energy spectrum discrete and mix the top and bottom Fermi arcs. We show that, in such films, the Fermi arcs become separated from the surface projections of the bulk states. To address the finite size effects on the bulk spectrum, we consider a simplified model of a doubly-degenerate triple-fold semimetal. For a thin film of this semimetal, both bulk and surface spectra are derived. Surface states show two branches, one of which is gapped. Using the obtained spectra, the density of states is analytically evaluated.

* gorbar@knu.ua

† pavlo.sukhachov@missouri.edu

This paper is organized as follows. The Fermi arcs in the two-node model of pseudospin-1 semimetals are studied in Sec. II. Finite size effects in thin films of triple-fold semimetals are considered in Section III. Our results are discussed and summarized in Sec. IV. Technical details of the wave function matching in triple-fold semimetals and vacuum are presented in Appendix A. Throughout this paper, we set $\hbar = 1$.

II. FERMI ARCS IN TWO-NODE MODEL

In Weyl semimetals, where the presence of an even number of Weyl nodes is a defining feature [53–55], the Fermi arc surface states connect the projections of the bulk Weyl nodes of opposite chiralities (topological numbers). To have a vanishing topological charge in the whole Brillouin zone, we also consider a model with two triple-fold nodes of opposite topological charges. We use the following low-energy model describing two triple-fold nodes:

$$\mathcal{H}_2 = \begin{pmatrix} 0 & iv_F k_x & -iv_F k_y \\ -iv_F k_x & 0 & i\gamma(k_z^2 - m) \\ iv_F k_y & -i\gamma(k_z^2 - m) & 0 \end{pmatrix}. \quad (1)$$

Its energy bands are

$$E_0 = 0, \quad E_{\pm} = \pm \sqrt{v_F^2(k_x^2 + k_y^2) + \gamma^2(k_z^2 - m)^2} \quad (2)$$

with the triple-fold nodes located at $k_z = \pm\sqrt{m}$. We plot this energy spectrum in Fig. 1 as a function of k_x and k_z . Note that Hamiltonian (1) defines a toy model which, while capturing the properties of triple-fold nodes, does not directly describe real materials such as CoSi. Yet, its simplicity is appealing because it allows us to get a glimpse into the main features of Fermi arcs and triple-fold fermions.

We consider Fermi arcs at the interface between a triple-fold semimetal and vacuum. The latter is modeled as a wide-gap insulator. To open a gap, we substitute first $m \rightarrow -M$ in Hamiltonian (1). Since the flat band still remains at zero energy, we shift the energy spectrum so that the Fermi energy is in the middle of one of the two band gaps by adding $\gamma M/2$. Thus, we obtain the following Hamiltonian for an insulating phase:

$$\mathcal{H}_2^{\text{gap}} = \mathcal{H}_2 \Big|_{m \rightarrow -M} + I_3 \frac{\gamma M}{2}. \quad (3)$$

Its eigenvalues are

$$E_0 = \frac{\gamma M}{2}, \quad E_{\pm} = \frac{\gamma M}{2} \pm \sqrt{v_F^2(k_x^2 + k_y^2) + \gamma^2(k_z^2 + M)^2}. \quad (4)$$

Hamiltonians (1) and (3) allow us to investigate the topological surface states of pseudospin-1 semimetals and

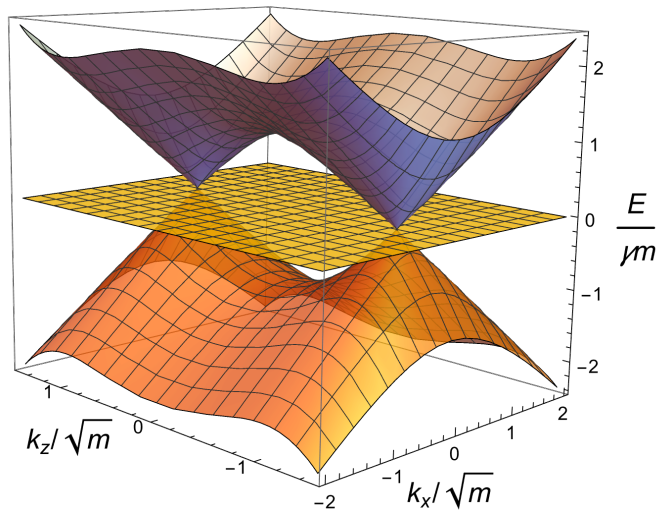


FIG. 1: The energy dispersion given in Eq. (2) in the model of 3D pseudospin-1 semimetal with two nodes as a function of k_x and k_z at $k_y = 0$. We set $v_F = \gamma\sqrt{m}$.

analyze their properties. For definiteness, we assume that the triple-fold semimetal is situated at $y < 0$ and the vacuum is at $y > 0$. The system is infinite in the x - and z -directions. In addition, we examine slabs of finite thickness L that are surrounded by vacuum on both sides.

A. Wave function matching

We begin with the simpler case of a semi-infinite semimetal. Given that Hamiltonian (1) is linear in k_y , naively, one would expect that straightforward matching of every component of the wave function on the semimetal-vacuum boundary will immediately provide the dispersion relation for the Fermi arc states. However, because of the flat band, the situation is more involved for triple-fold fermions.

In the model with Hamiltonian (3), vacuum flat band states cannot be matched with the bulk solutions at the interface for $E \neq \gamma M/2$. Consequently, the general solution contains one arbitrary constant related to the solution in vacuum and two in the semimetal. Therefore, matching of three-component wave functions yields a system of three equations for three unknown coefficients. Our analysis in Appendix A shows that this system has no non-trivial solutions.

The issue with matching arises due to an insufficient number of linearly independent solutions in vacuum to satisfy the matching conditions for a three-component wave function. To provide an additional solution, we consider a more realistic weakly-dispersing flat band by adding the following term to the Hamiltonian:

$$\mathcal{H}^{\text{quad}} = -\delta k_y^2 I_3, \quad (5)$$

where I_3 is the unit 3×3 matrix and $\delta \ll \gamma$ is a constant $\delta > 0$. [For simplicity, we ignore other quadratic terms,

see Ref. [56], for the full Hamiltonian of CoSi.] This term modifies the energy spectrum in vacuum as follows:

$$E_0 = \gamma \frac{M}{2} - \delta k_y^2, \quad (6)$$

$$E_{\pm} = \gamma \frac{M}{2} - \delta k_y^2 \pm \sqrt{v_F^2(k_x^2 + k_y^2) + \gamma^2(k_z^2 + M)^2} \quad (7)$$

We have the following eigenstate corresponding to E_0 in vacuum:

$$\psi_0 = \frac{1}{\sqrt{k_x^2 + k_y^2 + \gamma^2(k_z^2 + M)^2}} \begin{pmatrix} \gamma(k_z^2 + M) \\ k_y \\ k_x \end{pmatrix}, \quad (8)$$

where $k_y = \pm i \sqrt{(\gamma M - 2E)/(2\delta)}$ with $E < \frac{\gamma M}{2}$. In the limit $\delta \rightarrow 0$, we obtain

$$\psi_0 = \begin{pmatrix} 0 \\ 1 \\ 0 \end{pmatrix} + O(\sqrt{\delta}). \quad (9)$$

For E_{\pm} bands, the effect of the new quadratic term is negligible. In contrast, the correction has a qualitatively different impact on the flat band E_0 : a nonzero δ removes its degeneracy, inducing weak dispersion, such that for some values of k_y , the E_0 band states can attain the same energy as the dispersive eigenstates in the semimetal. Therefore, due to weak dispersion of the flat band, states in the semimetal and vacuum can be matched. According to Eq. (9), the second component of the wave function accounts for flat band states and in the case of an ideally flat band ($\delta = 0$) matching conditions are reduced to matching of only the first and third components.

Heuristically, this result also follows from requiring vanishing current through the interface $j_y = \psi^\dagger (\partial_{k_y} H) \psi$, which, as follows from Eq. (1), depends only on two components of the wave function ψ .

B. Surface states

To find the Fermi arcs, we use the approach described in Sec. II A. The energy dispersion of the top surface Fermi arc states is defined by the following characteristic equation:

$$\frac{v_F^2 k_x^2 - E^2}{Eq + k_x \gamma (k_z^2 - m)} = \frac{(E - \gamma M/2)^2 - v_F^2 k_x^2}{(E - \gamma M/2)p - k_x \gamma (k_z^2 + M)}, \quad (10)$$

where $v_F p = \sqrt{\gamma^2 (k_z^2 + M)^2 + v_F^2 k_x^2 - (E - \gamma M/2)^2}$ and $v_F q = \sqrt{\gamma^2 (k_z^2 - m)^2 + v_F^2 k_x^2 - E^2}$. Coefficients p

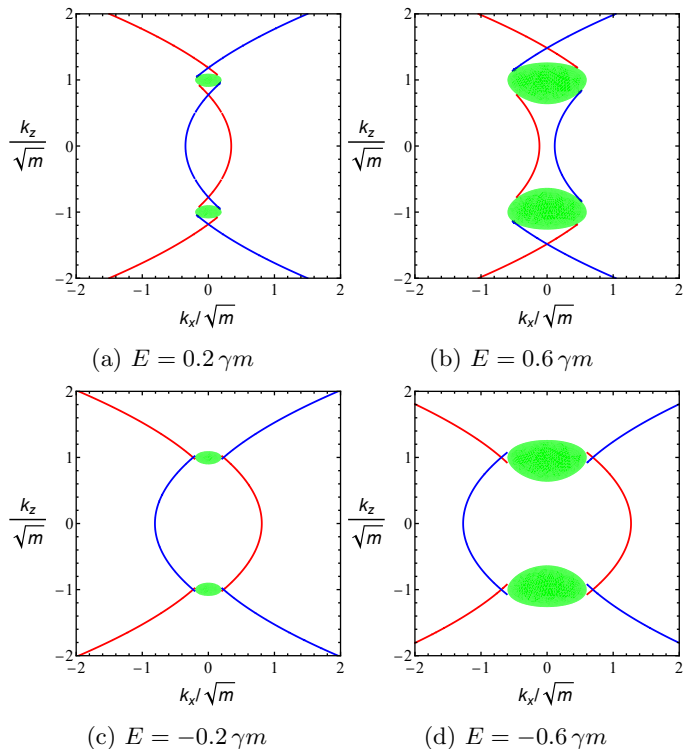


FIG. 2: Fermi arcs at the semimetal-vacuum interface for $v_F = \gamma\sqrt{m}$. Green regions represent the projections of the bulk spectrum onto the surface Brillouin zone.

Blue curves correspond to the bottom surface states, while red curves correspond to the top surface.

and q determine the inverse decay lengths in vacuum and semimetal, respectively.

In the limit $M \rightarrow \infty$, Eq. (10) simplifies as

$$\frac{v_F^2 k_x^2 - E^2}{Eq + k_x \gamma (k_z^2 - m)} = -\frac{v_F}{\sqrt{3}}, \quad (11)$$

leading to

$$E^2 = \frac{1}{4} \left[\sqrt{3} v_F k_x + \gamma (k_z^2 - m) \right]^2 \quad (12)$$

with the additional condition that $\sqrt{3}(v_F^2 k_x^2 - E^2) + v_F k_x \gamma (k_z^2 - m)$ is positive, which corresponds to surface states with positive energy on the top surface.

We present the Fermi arcs obtained from Eq. (12) in Fig. 2. One can see that there are Fermi arcs connecting the projections of the bulk spectrum onto the surface (at $k_z^2 < m$). In addition, there are Fermi arcs that go away from the projections of the Weyl nodes onto the surface Brillouin zone (at $k_z^2 > m$). We speculate that these arcs span the entire Brillouin zone. However, to study whether these Fermi arcs extend throughout the whole surface Brillouin zone, one should go beyond the effective low-energy model. We leave this question for further studies. As follows from Eq. (11), the Fermi arcs have a parabolic shape: the parts between the nodes and outside

the nodes are represented by the shifted parts of the same parabola that is cut perpendicular to its symmetry axis. Fermi arcs corresponding to the top (semimetal is in the $y < 0$ subspace) and bottom (semimetal is in the $y > 0$ subspace) surfaces are related by the mirror $k_x \rightarrow -k_x$ symmetry. In addition, both arcs are symmetric with respect to the $k_z = 0$ axis. Similar arcs were obtained numerically in Ref. [57]. On the other hand, Fermi arcs spanning outside the triple-fold nodes $k_z^2 > m$ are absent in a symmorphic toy model considered in Ref. [52].

The negative-energy Fermi arcs have a different shape in our model, cf. top and bottom panels in Fig. 2. This asymmetry originates from the particle-hole symmetry breaking of the Hamiltonian (3). Note that particle-hole symmetry could be preserved for a three-component Hamiltonian only if one band is completely flat and is located at zero energy. Therefore, gap opening necessarily breaks the particle-hole symmetry.

C. Hybridization of surface states in thin films

In the previous section, we considered a semi-infinite triple-fold semimetal. Real crystals are, of course, finite and are commonly grown as films. In sufficiently thin films, the overlap between the surface states can no longer be neglected and, as we show in this section, leads to the hybridization of the surface states.

Let us consider a slab of pseudospin-1 semimetal, which extends infinitely in the x - and z -directions and is contained within $-L/2 < y < L/2$ region. The electron states in the region outside the semimetal are described by the gapped Hamiltonian (3).

For the surface Fermi arc states, wavevector components k_x and k_z are good quantum numbers, and k_y is purely imaginary with its sign chosen such that wave functions exponentially decrease at infinity. This gives the following characteristic equation for the surface states:

$$\coth(qL) = -\frac{q(E - \gamma\frac{M}{2})}{2Ep} - \frac{Ep}{2(E - \gamma\frac{M}{2})q} + \frac{k_x^2\gamma^2(M + m)^2}{2(E - \gamma\frac{M}{2})Epq}. \quad (13)$$

Let us examine the relation in (13) in the limit of an infinitely large gap $M \rightarrow \infty$. Then, $p \rightarrow \sqrt{3}\gamma M/(2v_F)$ and we obtain

$$\coth(qL) = \frac{2E^2 - 3v_F^2k_x^2 + \gamma^2(k_z^2 - m)^2}{2\sqrt{3}Ev_Fq}. \quad (14)$$

In the limit of a thick slab $L \rightarrow \infty$, we have $\coth(qL) \rightarrow 1$ that gives

$$1 = \frac{2E^2 - 3v_F^2k_x^2 + \gamma^2(k_z^2 - m)^2}{2\sqrt{3}Ev_Fq}, \quad (15)$$

whose solutions reproduce the Fermi arcs described by Eq. (12) and presented in Fig. 2.

Using Eq. (14), we analyze how the thickness of the slab L affects surface states. We plot the corresponding solutions for Fermi arcs in Fig. 3 for a few values of energy and slab thickness. For illustrative purposes, we also add the projections of the bulk states of the semimetal at $L \rightarrow \infty$ shown by green regions. The finite size effects lead to the separation of the Fermi arcs into several parts. The qualitative behavior and reconnection of the arcs depend on the energy E . We separate two parameter regions: (i) $0 < E < \gamma m/2$ and (ii) $\gamma m/2 < E < \gamma m$. In the former case, the Fermi arcs at different surfaces of the thick slab have two intersections in momentum space at $k_z^2 < m$, see Fig. 2a. On the other hand, the arcs do not overlap in momentum space at $k_z^2 < m$ for $\gamma m/2 < E < \gamma m$, see Fig. 2b.

In the case $0 < E < \gamma m/2$, the finite size effects lead to the hybridization of the Fermi arcs and their separation into several parts: two V-shaped parts at $k_z^2 > m$, petal-like parts that surround the bulk-state projections, and a closed loop at $k_z^2 < m$. For $L < L_{\text{cr},1}$ with

$$L_{\text{cr},1} = \frac{2v_F}{\sqrt{3}E}, \quad (16)$$

the petal-like branches vanish first while the internal loop remains, see Figs. 3a and 3b. By further reducing L , we remove the central part, see Fig. 3c. The corresponding critical length is determined by

$$L_{\text{cr},2} = \frac{v_F}{\sqrt{\gamma^2 m^2 - E^2}} \operatorname{artanh} \left(\frac{2\sqrt{3}E\sqrt{\gamma^2 m^2 - E^2}}{2E^2 + \gamma^2 m^2} \right). \quad (17)$$

The order in which the petal-like curves and the central loop disappear depends on a further subdivision of the energy range: below the energy E_{sim} , defined by $L_{\text{cr},1}(E_{\text{sim}}) = L_{\text{cr},2}(E_{\text{sim}})$, the petal-like curves vanish first; above E_{sim} , the central loop disappears first. We numerically estimate $E_{\text{sim}} \approx 0.43\gamma m$.

In the second case with $\gamma m/2 < E < \gamma m$, $L_{\text{cr},2}$ defines a different lengthscale. The arcs reconnect in the central part for $L < L_{\text{cr},2}$ and form petal-like structures surrounding the projections of the bulk states, see Fig. 3e. Decreasing L below $L_{\text{cr},1}$ removes these petal-like structures, see Fig. 3f.

Therefore, thin films of triple-fold semimetals are expected to show intricate patterns of the surface states.

III. FINITE SIZE EFFECTS

A. Model

In the previous sections, we focused on the surface states in triple-fold semimetals. Let us now turn our attention to the finite size effects for bulk states. For this purpose, it would be enough to consider only the

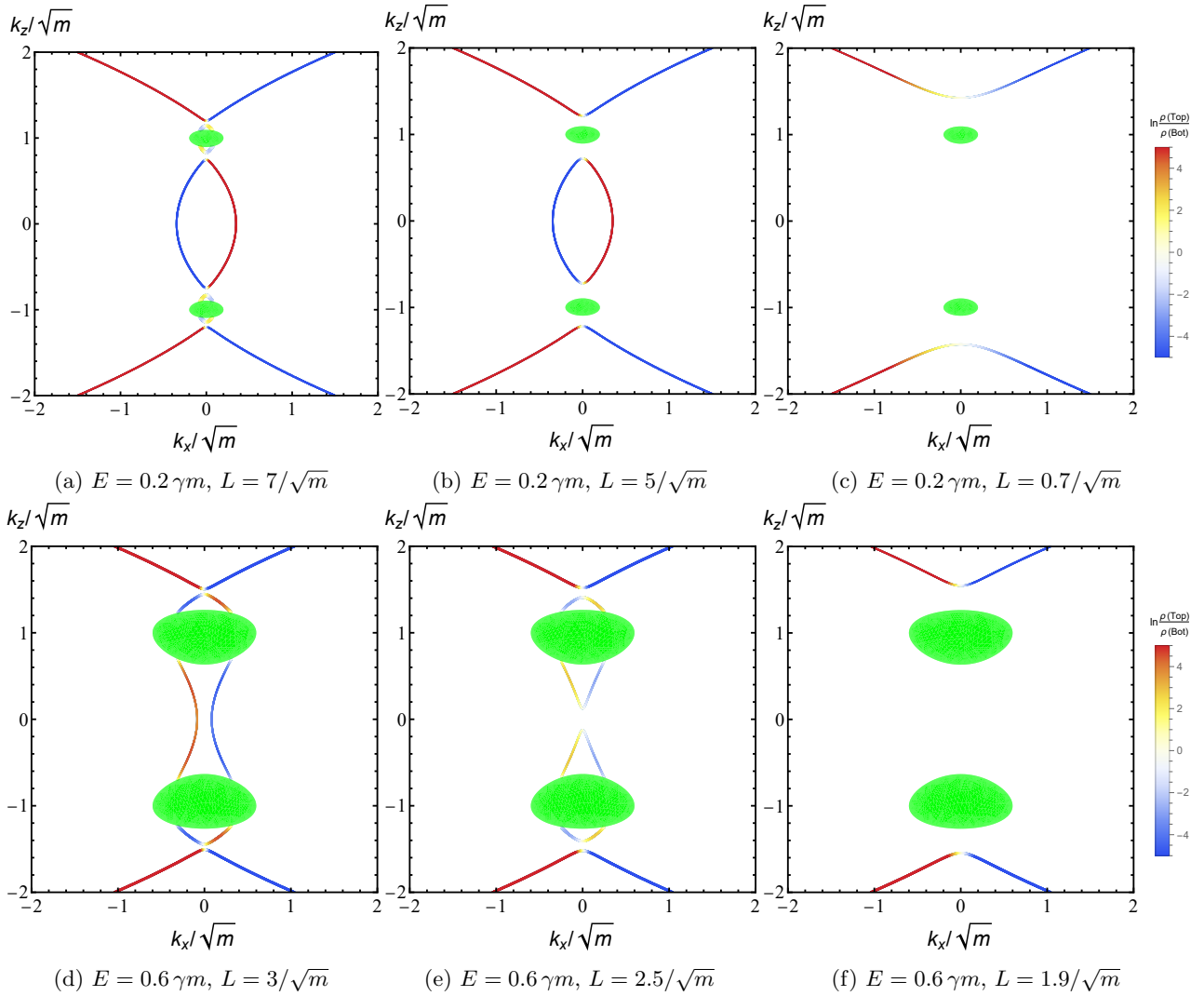


FIG. 3: Fermi arcs for a thin film of a triple-fold semimetal are shown as colored curves. The color indicates the spatial localization of the surface states: ρ_t and ρ_b are probability densities at the top and bottom surfaces, respectively. Points, whose value of $\ln(\rho_t/\rho_b)$ is above 4.5 (below -4.5), are still marked as red (blue). The projections of bulk states of semimetal at $L \rightarrow \infty$ are shown by green regions. In all panels, we fix $v_F = \gamma\sqrt{m}$.

low-energy states in the vicinity of the crossing points. Therefore, we adopt the following $\vec{k} \cdot \vec{p}$ Hamiltonian for pseudospin-1 fermions:

$$\mathcal{H}_0 = v_F \begin{pmatrix} 0 & ik_x & -ik_y \\ -ik_x & 0 & ik_z \\ ik_y & -ik_z & 0 \end{pmatrix} = v_F(\vec{S}_1 \cdot \vec{k}), \quad (18)$$

where

$$S_{1x} = \begin{pmatrix} 0 & i & 0 \\ -i & 0 & 0 \\ 0 & 0 & 0 \end{pmatrix}, S_{1y} = \begin{pmatrix} 0 & 0 & -i \\ 0 & 0 & 0 \\ i & 0 & 0 \end{pmatrix}, S_{1z} = \begin{pmatrix} 0 & 0 & 0 \\ 0 & 0 & i \\ 0 & -i & 0 \end{pmatrix} \quad (19)$$

are (pseudo)spin-1 matrices. In what follows, we will work with dimensionless parameters $E \rightarrow E/E_*$, $k \rightarrow k/k_*$ where E_* and k_* are characteristic energy and momentum. The characteristic momentum scale k_* is taken to be of the order of the inverse lattice constant, reflecting the typical scale at which the continuum approximation breaks down. The characteristic energy scale E_* is taken to be of the order of the energy at which deviations from the effective $\vec{k} \cdot \vec{p}$ Hamiltonian approximation become significant. For example, $E_* \sim \gamma m$ for the model given in Eq. (1). To simplify our notations, we take $v_F = E_*/k_*$.

To address finite-size effects, we consider a semimetal-vacuum interface. As in Sec. II, we model electron states in vacuum by introducing a gapped Hamiltonian. However, like for a single Weyl node, it is impossible to introduce an energy gap for the 3×3 Hamiltonian (18).

Therefore, we have to modify the model and consider a doubly degenerate triple-fold node. Before doing this, however, we find it instructive to prove why one cannot open a gap in the model given in Eq. (18).

A standard procedure to open a gap is to add a momentum-independent mass term to the Hamiltonian. The most general momentum-independent mass term in the case under consideration is given by the following

$$-E^3 + E^2(\mu_1 + \mu_2 + \mu_3) + E(k^2 + \alpha^2 + \beta^2 + \gamma^2 - \mu_1\mu_2 - \mu_2\mu_3 - \mu_1\mu_3) + (\mu_1\mu_2\mu_3 - \mu_1\gamma^2 - \mu_2\beta^2 - \mu_3\alpha^2 + 2\alpha\beta\gamma) - \mu_1k_z^2 - \mu_2k_y^2 - \mu_3k_x^2 - 2\beta k_x k_z - 2\alpha k_y k_z - 2\gamma k_x k_y = 0. \quad (21)$$

Since we can always shift the reference point for energy in Eq. (20), it is sufficient to show that a gap cannot be opened at $E = 0$. Therefore, it is sufficient to consider Eq. (21) at $E = 0$,

$$\begin{aligned} & \mu_1k_z^2 + \mu_2k_y^2 + \mu_3k_x^2 + 2\beta k_x k_z + 2\alpha k_y k_z + 2\gamma k_x k_y \\ & = \mu_1\mu_2\mu_3 - \mu_1\gamma^2 - \mu_2\beta^2 - \mu_3\alpha^2 + 2\alpha\beta\gamma. \end{aligned} \quad (22)$$

The gap is absent if Eq. (22) has a solution for a real-valued \mathbf{k} . To show that this is indeed the case, we rewrite Eq. (22) as follows:

$$k_i(\mathcal{H}_m)_{ij}k_j = \det \mathcal{H}_m. \quad (23)$$

Since $\det(\mathcal{H}_m) = \lambda_1\lambda_2\lambda_3$ is given by the product of eigenvalues of \mathcal{H}_m , applying an orthogonal transformation O , which diagonalizes matrix \mathcal{H}_m in Eq. (23), we arrive at

$$\lambda_1\tilde{k}_z^2 + \lambda_2\tilde{k}_y^2 + \lambda_3\tilde{k}_x^2 = \lambda_1\lambda_2\lambda_3, \quad (24)$$

where $\tilde{\mathbf{k}} = O\mathbf{k}$. It is easy to verify that there is always a solution to the above equation for any choice of λ_1 , λ_2 , and λ_3 . Therefore, we conclude that the gap cannot be opened at a single node of triple-fold semimetal via the mass term (20).

However, a gap can be opened by considering a system with degenerate bands and adding terms to the Hamiltonian that mix these bands. For pseudospin-1 semimetal with doubly degenerate bands defined by the Hamiltonian

$$\mathcal{H}_1 = \begin{pmatrix} \mathcal{H}_0 & 0 \\ 0 & \mathcal{H}_0^* \end{pmatrix} = (\vec{S}_1 \vec{k}) \otimes \tau_z, \quad (25)$$

an energy gap can be easily introduced by an off-diagonal mass term

$$\mathcal{H}_1^{\text{gap}} = \mathcal{H}_1 + \mu I_3 \otimes \tau_1. \quad (26)$$

Hermitian 3×3 matrix:

$$\mathcal{H}_m = \begin{pmatrix} \mu_1 & \alpha & \beta \\ \alpha & \mu_2 & \gamma \\ \beta & \gamma & \mu_3 \end{pmatrix}, \quad (20)$$

whose elements are real constants. In principle, the off-diagonal elements α , β , and γ could contain imaginary contributions; however, they can be easily absorbed by redefining the momenta components k_x , k_y , and k_z in the low-energy Hamiltonian (18). Eigenvalues of $\mathcal{H}_0 + \mathcal{H}_m$ are determined by the following characteristic equation:

As we discussed in Sec. II A, only four out of six components of wave functions should be matched at boundaries. For the surface of the semimetal at $y = 0$, we derive the following dispersion relation for the surface states:

$$4E^2(k_x^2 + k_z^2 - E^2)^2 = \mu^2(k_x^2 + k_z^2 - 2E^2)^2. \quad (27)$$

In the $\mu \rightarrow \infty$ limit, we get

$$E = \pm \frac{k_{\parallel}}{\sqrt{2}}, \quad (28)$$

where $k_{\parallel} = \sqrt{k_x^2 + k_z^2}$. Therefore, unlike the case in Sec. II, we have a circular surface state.

B. Characteristic equation and energy spectrum

To address the finite size effects, we consider a slab of semimetal embedded in vacuum whose electron states are described by Hamiltonians (25) and (26), respectively, with the same orientation of the slab as in Sec. II C. In this setup, the semimetal is at $-L/2 < y < L/2$, hence k_x and k_z are good quantum numbers. The inverse decay lengths are determined by $q = \sqrt{k_x^2 + k_z^2 - E^2}$ and $p = \sqrt{\mu^2 - E^2 + k_x^2 + k_z^2}$.

By matching the wave functions at boundaries and separating decaying in the bulk states from the propagating ones, we obtain the following characteristic equations for the surface states:

$$2 \coth(qL) = \frac{E p^2 E^2 - q^2 \epsilon^2}{\epsilon q p E \epsilon} \pm \frac{\mu p^2 E^2 + q^2 \epsilon^2}{\epsilon q p E \epsilon}, \quad (29)$$

where $\epsilon = \sqrt{\mu^2 - E^2}$. The characteristic equation for bulk states can be obtained by substituting $q = il$, $l =$

$\sqrt{E^2 - k_x^2 - k_z^2}$ in Eq. (29), leading to

$$2 \cot(lL) = \frac{E p^2 E^2 + l^2 \epsilon^2}{\epsilon l p E \epsilon} \pm \frac{\mu p^2 E^2 - l^2 \epsilon^2}{\epsilon l p E \epsilon}. \quad (30)$$

In the limit $\mu \rightarrow \infty$, the characteristic equation is reduced to

$$\coth\left(L\sqrt{k_x^2 + k_z^2 - E^2}\right) = \pm \frac{k_x^2 + k_z^2}{2E\sqrt{k_x^2 + k_z^2 - E^2}} \quad (31)$$

$$\cot\left(L\sqrt{E^2 - k_x^2 - k_z^2}\right) = \pm \frac{k_x^2 + k_z^2}{2E\sqrt{E^2 - k_x^2 - k_z^2}} \quad (32)$$

at $E^2 < k_x^2 + k_z^2$ and $E^2 > k_x^2 + k_z^2$, respectively.

The dispersion relation of the flat band is not modified in this model, and the only finite-size effect of the system is the quantization of momentum component perpendicular to the surfaces $k_y = \pi n/L$, $n \in \mathbb{N}$.

The energy spectrum defined by Eqs. (31) and (32) is plotted in Fig. 4 for $L = 10$ (measured in the units of $1/k_*$). The bulk energy spectrum is quantized with the finite-size gap given by $\Delta E_{\text{gap}} = \pi/(2L)$. The bulk states appear in pairs of branches, corresponding to the \pm sign in Eq. (30). The distance between quantized energy levels is given by π/L . While most of the bulk energy levels extend indefinitely, the ground energy level deviates from this behavior: at $k_{\parallel} = 2/L$, it smoothly connects to the surface-state branch. We also note that there are always two branches of surface-localized modes. The key distinction between them lies in the internal structure of the wave function. To make this explicit, consider the six-component (spinor) functions $\psi_t \propto e^{qy}$, localized on the top surface, and, respectively, $\psi_b \propto e^{-qy}$, localized on the bottom surface. These functions are related by the symmetry transformation

$$\psi_t = \begin{pmatrix} 0 & I_3 \\ I_3 & 0 \end{pmatrix} \hat{T} \hat{E} \hat{M}_y \psi_b, \quad (33)$$

where \hat{T} is the time reversal operator, \hat{E} changes the sign of energy, \hat{M}_y is the mirror reflection about the $y = 0$ plane, and the prefactor matrix represents the valley-exchange operation. One can verify that this relation implies $\psi_b^\dagger \psi_b e^{2qy} = \psi_t^\dagger \psi_t e^{-2qy}$, preserving normalization under reflection.

The main distinction between the two branches, which correspond to the gapped (upper) and gapless (lower) surface states, lies in their construction. For the gapped branch, the total wave function within the region $-L/2 < y < L/2$ is given by $\Psi = \psi_b + \psi_t$, whereas for the gapless branch it takes the form $\Psi = \psi_b - \psi_t$. The explicit structure of ψ_b and ψ_t depends not only on the energy E and magnitude of the in-plane momentum k_{\parallel} but also on its direction.

The energy–momentum relation, expressed as a function of the magnitude of in-plane momentum k_{\parallel} , is characterized by families of curves that exhibit linear asymptotic behavior. Specifically, bulk states approach the

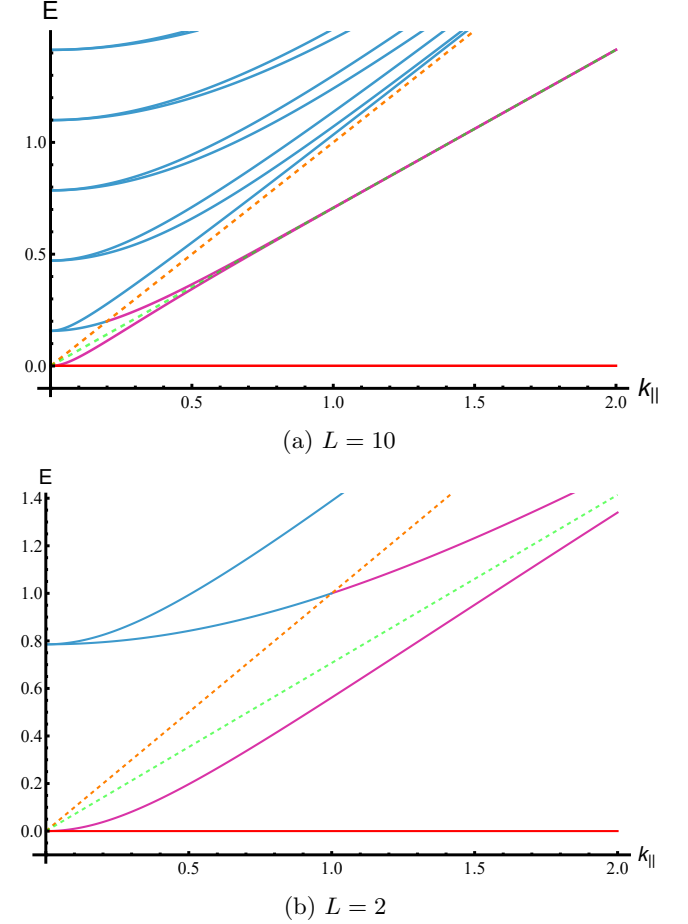


FIG. 4: Energy spectrum ($E \geq 0$) of a slab of doubly-degenerate triple-fold semimetal with finite thickness L at $\mu \rightarrow \infty$ defined by Eqs. (31) and (32). The states above the orange dotted line correspond to bulk states (blue lines), while below that line, only surface states are possible, which are plotted in magenta. The flat band is plotted in red. The green dotted line represents the surface Dirac cone, which appears in the $L \rightarrow \infty$ limit.

asymptote $E = k_{\parallel}$, while surface-localized states approach $E = k_{\parallel}/\sqrt{2}$. Near $k_{\parallel} = 0$, these curves can be well-approximated by a quadratic dependence. All bulk state branches eventually asymptotically approach the $E = k_{\parallel}$ line. Thus, branches with equal energy gaps (pairs of solutions of Eq. (30) with \pm sign) converge at $k_{\parallel} \rightarrow \infty$. Across the full momentum range, they are captured by branches of hyperbolas:

$$E = \begin{cases} \frac{1}{2}\sqrt{\frac{\pi^2}{L^2} + 2k_{\parallel}^2} - \frac{\pi^2}{2L^2\sqrt{\frac{\pi^2}{L^2} + 2k_{\parallel}^2}}, & \text{for gapless surface branch,} \\ \frac{1}{2}\sqrt{\frac{\pi^2}{L^2} + 2k_{\parallel}^2}, & \text{for ground-state bulk branch and gapped surface branch,} \\ \frac{1}{2}\sqrt{\frac{\pi^2(2n-1)^2}{L^2} + 4k_{\parallel}^2}, & \text{for the } n\text{-th pair of bulk branches.} \end{cases} \quad (34)$$

The hyperbolic approximation described above is applicable in the regions between each such pair of branches. This symmetric placement reduces error in estimating the density of states. The densities of the bulk

and surface states are calculated in this approximation without taking the spin degeneracy into account, and the result reads

$$N_{\text{bulk}}(E) = \frac{E}{\pi v_F^2} \left[\frac{1}{2}\theta\left(E - \frac{\pi v_F}{2L}\right) - \theta\left(E - \frac{2v_F}{L}\right) + \sum_{n=1}^{\infty} \theta\left(E - \frac{\pi(2n-1)v_F}{2L}\right) \right], \quad (35)$$

$$N_{\text{surface}}(E) = \frac{E}{\pi v_F^2} \theta\left(E - \frac{2v_F}{L}\right) + \frac{1}{2\pi v_F^2} \left(E + \sqrt{E^2 + \frac{\pi^2 v_F^2}{L^2}} + \frac{E^2}{\sqrt{E^2 + \frac{\pi^2 v_F^2}{L^2}}} \right) \theta(E), \quad (36)$$

where $\theta(x)$ denotes the unit step function and we restored v_F .

IV. SUMMARY

We analytically studied topological surface states in 3D triple-fold semimetals in the two-node continuum model, and addressed the finite-size effects in a continuum model of a doubly degenerate triple-fold semimetal.

It was found that the matching of wavefunctions at the semimetal-vacuum interface is peculiar for triple-fold semimetals in view of the presence of a flat band. In particular, we showed that only two out of three wavefunction components should be matched at the interface. Heuristically, this result can be inferred by requiring that the current normal to the interface vanishes because it involves only two out of three components of the wave functions. The same conclusion can be reached by including a weak dispersion for the flat band.

In agreement with the topological charge arguments, we found that there exist two Fermi arcs per triple-fold node. While one Fermi arc connects two nodes, the other radiates away and is reminiscent of the long Fermi arc spanning the whole Brillouin zone observed in CoSi [41–43], see Fig. 2.

In thin films of triple-fold semimetals, the surface states which belong to different surfaces hybridize, see Eq. (13) for the characteristic equation. Depending on the energy and the semimetal thickness, a few scenarios are possible for the Fermi arc hybridization. For $0 < E < \gamma m/2$, two petal-like curves connecting surface projections of bulk triple-fold nodes and a closed loop separated from the petal-like curves are realised, see Fig. 3a. The central loop is absent for $\gamma m/2 < E < \gamma m$,

see Fig. 3d.

Our study of finite size effects in slabs of doubly degenerate triple-fold materials revealed that the dispersive bands become quantized with the distance between the levels determined by the thickness of the slab, see Eq. (32) for the corresponding characteristic equation. In addition to these bulk modes, we also found two surface-localized states with isotropic Dirac dispersion. One of these states is purely surface-localized, while the other transitions into the bulk state, see Fig. 4.

The obtained results will be instrumental for investigating thin films of multi-fold semimetals. In particular, the nontrivial shape of the arcs and the quantization of the bulk states can be accessed via angle-resolved photoemission spectroscopy, scanning tunneling spectroscopy, and optical responses.

ACKNOWLEDGMENTS

A.Yu.P. and E.V.G. acknowledge support from the National Research Foundation of Ukraine grant (2023.03/0097) “Electronic and transport properties of Dirac materials and Josephson junctions”. P.O.S. thanks the Center for Quantum Spintronics (QuSpin) for warm hospitality, where this work was finalized.

Appendix A: Wave function matching

In this appendix, we provide technical details of the wave function matching at the interface between the triple-fold semimetal and vacuum. We use the model Hamiltonians given in Eqs. (1) and (3) in triple-fold semimetal and vacuum, respectively.

The eigenstates of the system with energy E are defined by

$$\begin{pmatrix} \gamma\tilde{M}(y) & iv_F k_x & -v_F \partial_y \\ -iv_F k_x & \gamma\tilde{M}(y) & i\gamma [k_z^2 - \tilde{m}(y)] \\ v_F \partial_y & -i\gamma [k_z^2 - \tilde{m}(y)] & \gamma\tilde{M}(y) \end{pmatrix} \Psi = E\Psi \quad (\text{A1})$$

with position-dependent parameters

$$\tilde{m}(y) = \begin{cases} -M, & y > 0, \\ m, & y < 0, \end{cases} \quad \tilde{M}(y) = \begin{cases} \frac{M}{2}, & y > 0, \\ 0, & y < 0. \end{cases} \quad (\text{A2})$$

In view of the translation invariance in the x and z directions, we seek eigenstates as plane waves with momenta k_x and k_z . Then the general solution to Eq. (A1) for bulk states with $q \neq 0$ is given by

$$\Psi = e^{i(k_x x + i k_z z)} \begin{cases} C_1 \begin{pmatrix} v_F k_x \gamma (k_z^2 - m) + iv_F q E \\ v_F^2 q k_x - i\gamma (k_z^2 - m) E \\ -E^2 + v_F^2 k_x^2 \end{pmatrix} e^{iqy} + C_2 \begin{pmatrix} v_F k_x \gamma (k_z^2 - m) - iv_F q E \\ -v_F^2 q k_x - i\gamma (k_z^2 - m) E \\ -E^2 + v_F^2 k_x^2 \end{pmatrix} e^{-iqy}, & y < 0, \\ C_3 \begin{pmatrix} v_F k_x \gamma (k_z^2 + M) - v_F p (E - \gamma \frac{M}{2}) \\ iv_F^2 p k_x - i\gamma (k_z^2 + M) (E - \gamma \frac{M}{2}) \\ -(E - \gamma \frac{M}{2})^2 + v_F^2 k_x^2 \end{pmatrix} e^{-py}, & y > 0, \end{cases} \quad (\text{A3})$$

where C_1, C_2, C_3 are arbitrary constants and

$$v_F q = \sqrt{E^2 - \gamma^2 (k_z^2 - m)^2 - v_F^2 k_x^2}, \quad v_F p = \sqrt{\gamma^2 (k_z^2 + M)^2 + v_F^2 k_x^2 - \left(E - \gamma \frac{M}{2}\right)^2}. \quad (\text{A4})$$

Matching all three components of the wave function at the interface $y = 0$ results in the following system of three linear homogeneous equations for C_1, C_2 , and C_3 :

$$\begin{cases} (-E^2 + v_F^2 k_x^2)(C_1 + C_2) = \left[-(E - \gamma \frac{M}{2})^2 + v_F^2 k_x^2\right] C_3, \\ k_x \gamma (k_z^2 - m)(C_1 + C_2) + iqE(C_1 - C_2) = [k_x \gamma (k_z^2 + M) - p(E - \gamma \frac{M}{2})] C_3, \\ v_F^2 q k_x (C_1 - C_2) - i\gamma (k_z^2 - m) E (C_1 + C_2) = [iv_F^2 p k_x - i\gamma (k_z^2 + M) (E - \gamma \frac{M}{2})] C_3. \end{cases} \quad (\text{A5})$$

Nontrivial solutions to this system exist when its determinant equals zero. In the limit $M \rightarrow \infty$, the determinant takes the form

$$q \left\{ v_F^2 k_x^2 \gamma (k_z^2 + M) + v_F^2 p k_x \gamma \frac{M}{2} - E \gamma (k_z^2 + M) \left(E - \gamma \frac{M}{2}\right) - \gamma (k_z^2 - m) \left[v_F^2 k_x^2 - \left(E - \gamma \frac{M}{2}\right)^2 \right] \right\} \xrightarrow{M \rightarrow \infty} \frac{1}{4} \gamma^2 M^2 q \left[2E + \sqrt{3} v_F k_x + \gamma (k_z^2 - m) \right]. \quad (\text{A6})$$

This determinant vanishes for $q = 0$, leading to a solution which grows linearly with y and is not normalized. As a result, the solution for $y < 0$ contains only one arbitrary constant, making it trivial to show that the matching conditions cannot be satisfied. At $q \neq 0$, the expression in the square brackets vanishes only at $E = -[\sqrt{3} v_F k_x + \gamma (k_z^2 - m)]/2$. However, in this case,

$$v_F q = \sqrt{\frac{3}{4} v_F^2 k_x^2 + \frac{\sqrt{3}}{2} v_F k_x \gamma (k_z^2 - m) + \frac{1}{4} \gamma^2 (k_z^2 - m)^2 - \gamma^2 (k_z^2 - m)^2 - v_F^2 k_x^2} = \frac{1}{2} \sqrt{-\left(\sqrt{3} \gamma (k_z^2 - m) - v_F k_x\right)^2}$$

is purely imaginary; hence, it cannot correspond to bulk states. Furthermore, in view of the structure of the wave function in Eq. (A3), this solution does not correspond to normalizable surface states.

Thus, the system admits only the trivial solution, which shows that the matching of all components of the wave function across the semimetal-vacuum interface is not possible.

Appendix B: Dependence of surface spectrum on mass parameter

Let us address the dependence of the dispersion relation on the mass parameter μ , focusing on the surface states in the thin film. This parameter should be of the order of the work function, which is typically in the eV range. While typical values of characteristic energy should be in the range of 1 meV - 100 meV, it is important to verify that the limit $\mu \rightarrow \infty$ yields reliable results within this interval.

We compare the energy spectrum of the surface states in the infinite gap limit $\mu \rightarrow \infty$ with its counterpart for a finite gap in Fig. 5. For realistic values of the gap, the surface state spectrum is in good agreement with its counterpart in the infinite mass limit.

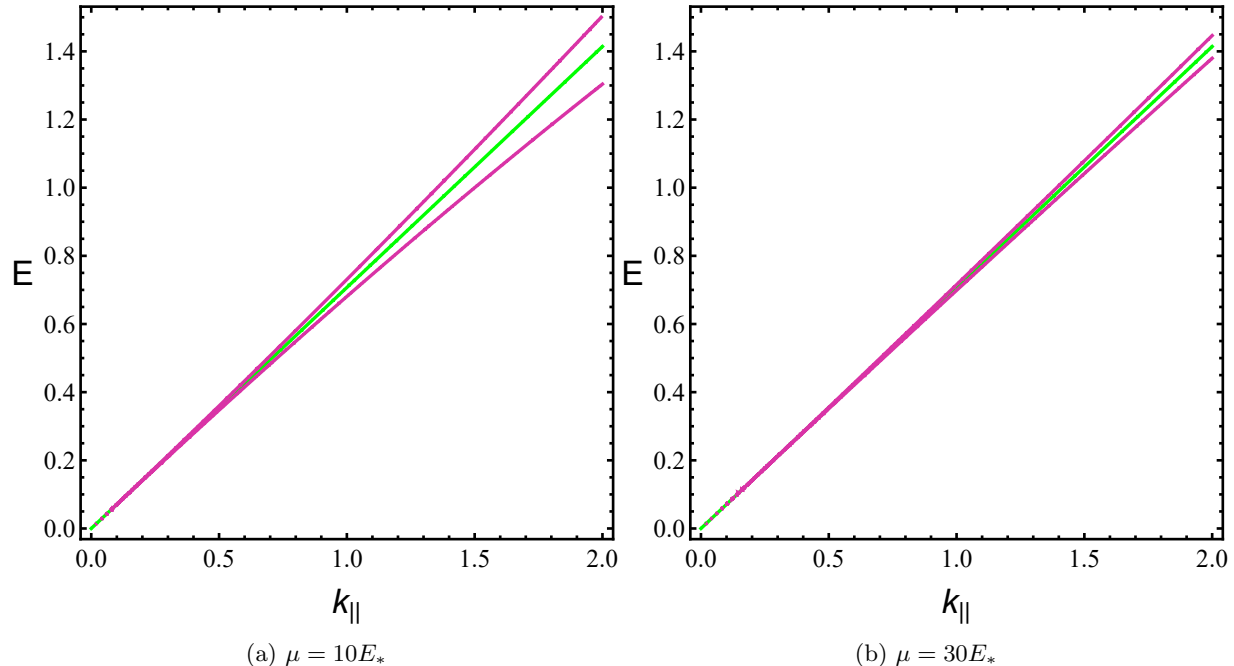


FIG. 5: Dispersion relation of surface states given in Eq. (27) for finite values of gap parameter μ (pink) and at $\mu \rightarrow \infty$ (green). We use the dimensionless variables, see the text after Eq. (19) for the definition.

As is evident from Fig. 5, for small values of momentum, where the finite-size effects are the strongest, the influence of the finite gap is negligible. Therefore, the infinite mass assumptions made during the investigation of surface states and finite size effects were justified.

-
-
- [1] Z. K. Liu, B. Zhou, Y. Zhang, Z. J. Wang, H. M. Weng, D. Prabhakaran, S.-K. Mo, Z. X. Shen, Z. Fang, X. Dai, Z. Hussain, and Y. L. Chen, Discovery of a three-dimensional topological Dirac semimetal, *Na₃Bi*, *Science* **343**, 864 (2014), [arXiv:1310.0391](#).
 - [2] S. Borisenko, Q. Gibson, D. Evtushinsky, V. Zabolotnyy, B. Büchner, and R. J. Cava, Experimental realization of a three-dimensional Dirac semimetal, *Phys. Rev. Lett.* **113**, 027603 (2014), [arXiv:1309.7978](#).
 - [3] Z. K. Liu, J. Jiang, B. Zhou, Z. J. Wang, Y. Zhang, H. M. Weng, D. Prabhakaran, S.-K. Mo, H. Peng, P. Dudin, T. Kim, M. Hoesch, Z. Fang, X. Dai, Z. X. Shen, D. L. Feng, Z. Hussain, and Y. L. Chen, A stable three-dimensional topological Dirac semimetal *Cd₃As₂*, *Nat. Mater.* **13**, 677 (2014).
 - [4] M. Neupane, S.-Y. Xu, R. Sankar, N. Alidoust, G. Bian, C. Liu, I. Belopolski, T.-R. Chang, H.-T. Jeng, H. Lin, A. Bansil, F. Chou, and M. Z. Hasan, Observation of a three-dimensional topological Dirac semimetal phase in high-mobility *Cd₃As₂*, *Nat. Commun.* **5**, 3786 (2014), [arXiv:1309.7892](#).
 - [5] S.-Y. Xu, C. Liu, S. K. Kushwaha, R. Sankar, J. W. Krizan, I. Belopolski, M. Neupane, G. Bian, N. Alidoust, T.-R. Chang, H.-T. Jeng, C.-Y. Huang, W.-F. Tsai, H. Lin, P. P. Shibayev, F.-C. Chou, R. J. Cava, and M. Z. Hasan, Observation of Fermi arc surface states in a topological metal, *Science* **347**, 294 (2015), [arXiv:1501.01249](#).
 - [6] A. Liang, C. Chen, Z. Wang, Y. Shi, Y. Feng, H. Yi,

- Z. Xie, S. He, J. He, Y. Peng, Y. Liu, D. Liu, C. Hu, L. Zhao, G. Liu, X. Dong, J. Zhang, M. Nakatake, H. Iwasawa, K. Shimada, M. Arita, H. Namatame, M. Taniguchi, Z. Xu, C. Chen, H. Weng, X. Dai, Z. Fang, and X.-J. Zhou, Electronic structure, Dirac points and Fermi arc surface states in three-dimensional Dirac semimetal Na_3Bi from angle-resolved photoemission spectroscopy, *Chin. Phys. B* **25**, 077101 (2016).
- [7] H. Weng, C. Fang, Z. Fang, B. A. Bernevig, and X. Dai, Weyl semimetal phase in noncentrosymmetric transition-metal monophosphides, *Phys. Rev. X* **5**, 011029 (2015), [arXiv:1501.00060](#).
- [8] S.-M. Huang, S.-Y. Xu, I. Belopolski, C.-C. Lee, G. Chang, B. Wang, N. Alidoust, G. Bian, M. Neupane, C. Zhang, S. Jia, A. Bansil, H. Lin, and M. Z. Hasan, A Weyl fermion semimetal with surface Fermi arcs in the transition metal monpnictide TaAs class, *Nat. Commun.* **6**, 7373 (2015), [arXiv:1501.00755](#).
- [9] C.-C. Lee, S.-Y. Xu, S.-M. Huang, D. S. Sanchez, I. Belopolski, G. Chang, G. Bian, N. Alidoust, H. Zheng, M. Neupane, B. Wang, A. Bansil, M. Z. Hasan, and H. Lin, Fermi surface interconnectivity and topology in Weyl fermion semimetals TaAs, TaP, NbAs, and NbP, *Phys. Rev. B* **92**, 235104 (2015), [arXiv:1508.05999](#) [[cond-mat.mes-hall](#)].
- [10] Y. Sun, S.-C. Wu, and B. Yan, Topological surface states and Fermi arcs of the noncentrosymmetric Weyl semimetals TaAs, TaP, NbAs, and NbP, *Phys. Rev. B* **92**, 115428 (2015), [arXiv:1508.06649](#).
- [11] Z. K. Liu, L. X. Yang, Y. Sun, T. Zhang, H. Peng, H. F. Yang, C. Chen, Y. Zhang, Y. F. Guo, D. Prabhakaran, M. Schmidt, Z. Hussain, S. K. Mo, C. Felser, B. Yan, and Y. L. Chen, Evolution of the Fermi surface of Weyl semimetals in the transition metal pnictide family, *Nat. Mater.* **15**, 27 (2016).
- [12] I. Belopolski, S.-Y. Xu, D. S. Sanchez, G. Chang, C. Guo, M. Neupane, H. Zheng, C.-C. Lee, S.-M. Huang, G. Bian, N. Alidoust, T.-R. Chang, B. Wang, X. Zhang, A. Bansil, H.-T. Jeng, H. Lin, S. Jia, and M. Z. Hasan, Criteria for Directly Detecting Topological Fermi Arcs in Weyl Semimetals, *Phys. Rev. Lett.* **116**, 066802 (2016), [arXiv:1601.04327](#).
- [13] F. Arnold, M. Naumann, S.-C. Wu, Y. Sun, M. Schmidt, H. Borrmann, C. Felser, B. Yan, and E. Hassinger, Chiral Weyl pockets and Fermi surface topology of the Weyl semimetal TaAs, *Phys. Rev. Lett.* **117**, 146401 (2016), [arXiv:1603.08846](#).
- [14] A. M. Turner and A. Vishwanath, *Beyond Band Insulators: Topology of Semi-Metals and Interacting Phases*, edited by M. Franz and L. Molenkamp (Elsevier Science, Amsterdam, 2013) [arXiv:1301.0330](#).
- [15] T. Wehling, A. Black-Schaffer, and A. Balatsky, Dirac materials, *Adv. Phys.* **63**, 1 (2014), [arXiv:1405.5774](#).
- [16] B. Yan and C. Felser, Topological materials: Weyl semimetals, *Annu. Rev. Condens. Matter Phys.* **8**, 337 (2017), [arXiv:1611.04182](#).
- [17] M. Z. Hasan, S.-Y. Xu, I. Belopolski, and S.-M. Huang, Discovery of Weyl fermion semimetals and topological Fermi arc states, *Annu. Rev. Condens. Matter Phys.* **8**, 289 (2017), [arXiv:1702.07310](#).
- [18] A. Burkov, Weyl Metals, *Annu. Rev. Condens. Matter Phys.* **9**, 359 (2018), [arXiv:1704.06660](#).
- [19] N. P. Armitage, E. J. Mele, and A. Vishwanath, Weyl and Dirac semimetals in three-dimensional solids, *Rev. Mod. Phys.* **90**, 015001 (2018), [arXiv:1705.01111](#).
- [20] E. V. Gorbar, V. A. Miransky, I. A. Shovkovy, and P. O. Sukhachov, *Electronic Properties of Dirac and Weyl Semimetals* (World Scientific, Singapore, 2021).
- [21] S. L. Adler, Axial-Vector Vertex in Spinor Electrodynamics, *Phys. Rev.* **177**, 2426 (1969).
- [22] J. S. Bell and R. Jackiw, A PCAC puzzle: $\pi_0 \rightarrow \gamma\gamma$ in the σ -model, *Il Nuovo Cimento A* **60**, 47 (1969).
- [23] H. Nielsen and M. Ninomiya, The Adler-Bell-Jackiw anomaly and Weyl fermions in a crystal, *Phys. Lett. B* **130**, 389 (1983).
- [24] X. Huang, L. Zhao, Y. Long, P. Wang, D. Chen, Z. Yang, H. Liang, M. Xue, H. Weng, Z. Fang, X. Dai, and G. Chen, Observation of the chiral-anomaly-induced negative magnetoresistance in 3D Weyl semimetal TaAs, *Phys. Rev. X* **5**, 031023 (2015), [arXiv:1503.01304](#).
- [25] X. Yang, Y. Liu, Z. Wang, Y. Zheng, and Z.-a. Xu, Chiral anomaly induced negative magnetoresistance in topological Weyl semimetal NbAs (2015), [arXiv:1506.03190](#).
- [26] C.-L. Zhang, S.-Y. Xu, I. Belopolski, Z. Yuan, Z. Lin, B. Tong, G. Bian, N. Alidoust, C.-C. Lee, S.-M. Huang, T.-R. Chang, G. Chang, C.-H. Hsu, H.-T. Jeng, M. Neupane, D. S. Sanchez, H. Zheng, J. Wang, H. Lin, C. Zhang, H.-Z. Lu, S.-Q. Shen, T. Neupert, M. Zahid Hasan, and S. Jia, Signatures of the Adler-Bell-Jackiw chiral anomaly in a Weyl fermion semimetal, *Nat. Commun.* **7**, 10735 (2016), [arXiv:1601.04208](#).
- [27] J. Du, H. Wang, Q. Chen, Q. Mao, R. Khan, B. Xu, Y. Zhou, Y. Zhang, J. Yang, B. Chen, C. Feng, and M. Fang, Large unsaturated positive and negative magnetoresistance in Weyl semimetal TaP, *Sci. China Phys. Mech. Astron.* **59**, 657406 (2016), [arXiv:1507.05246](#).
- [28] Z. Wang, Y. Zheng, Z. Shen, Y. Lu, H. Fang, F. Sheng, Y. Zhou, X. Yang, Y. Li, C. Feng, and Z.-A. Xu, Helicity-protected ultrahigh mobility Weyl fermions in NbP, *Phys. Rev. B* **93**, 121112 (2016), [arXiv:1506.00924](#).
- [29] Y. Li, Z. Wang, P. Li, X. Yang, Z. Shen, F. Sheng, X. Li, Y. Lu, Y. Zheng, and Z.-A. Xu, Negative magnetoresistance in Weyl semimetals NbAs and NbP: Intrinsic chiral anomaly and extrinsic effects, *Front. Phys.* **12**, 127205 (2017), [arXiv:1612.04031](#).
- [30] B. Bradlyn, J. Cano, Z. Wang, M. G. Vergniory, C. Felser, R. J. Cava, and B. A. Bernevig, Beyond Dirac and Weyl fermions: Unconventional quasiparticles in conventional crystals, *Science* **353**, aaf5037 (2016), [arXiv:1603.03093](#).
- [31] Z. Zhu, G. W. Winkler, Q. Wu, J. Li, and A. A. Soluyanov, Triple Point Topological Metals, *Phys. Rev. X* **6**, 031003 (2016), [arXiv:1605.04653](#).
- [32] I. Szyoz, Statistics of Kagome Lattice, *Prog. Theor. Phys.* **6**, 306 (1951).
- [33] B. Sutherland, Localization of electronic wave functions due to local topology, *Phys. Rev. B* **34**, 5208 (1986).
- [34] J. Vidal, R. Mosseri, and B. Douçot, Aharonov-Bohm Cages in Two-Dimensional Structures, *Phys. Rev. Lett.* **81**, 5888 (1998), [arXiv:cond-mat/9806068](#).
- [35] E. H. Lieb, Two theorems on the Hubbard model, *Phys. Rev. Lett.* **62**, 1201 (1989).
- [36] A. Raoux, M. Morigi, J.-N. Fuchs, F. Piéchon, and G. Montambaux, From Dia- to Paramagnetic Orbital Susceptibility of Massless Fermions, *Phys. Rev. Lett.* **112**, 026402 (2014), [arXiv:1306.6824](#).
- [37] Á. D. Kovács, G. Dávid, B. Dóra, and J. Cserti,

- Frequency-dependent magneto-optical conductivity in the generalized $\alpha - T_3$ model, *Phys. Rev. B* **95**, 035414 (2017), [arXiv:1605.09588](#).
- [38] A. Iurov, G. Gumbs, and D. Huang, Peculiar electronic states, symmetries, and Berry phases in irradiated $\alpha - T_3$ materials, *Phys. Rev. B* **99**, 205135 (2019), [arXiv:1806.09172](#).
- [39] A. Iurov, L. Zhemchuzhna, G. Gumbs, and D. Huang, Optical conductivity of gapped $\alpha - T_3$ materials with a deformed flat band, *Physical Review B* **107**, 195137 (2023).
- [40] C.-D. Han and Y.-C. Lai, Optical response of two-dimensional Dirac materials with a flat band, *Phys. Rev. B* **105**, 155405 (2022), [arXiv:2203.17161](#).
- [41] D. Takane, Z. Wang, S. Souma, K. Nakayama, T. Nakamura, H. Oinuma, Y. Nakata, H. Iwasawa, C. Cacho, T. Kim, K. Horiba, H. Kumigashira, T. Takahashi, Y. Ando, and T. Sato, Observation of Chiral Fermions with a Large Topological Charge and Associated Fermi-Arc Surface States in CoSi, *Phys. Rev. Lett.* **122**, 076402 (2019), [arXiv:1809.01312](#).
- [42] Z. Rao, H. Li, T. Zhang, S. Tian, C. Li, B. Fu, C. Tang, L. Wang, Z. Li, W. Fan, J. Li, Y. Huang, Z. Liu, Y. Long, C. Fang, H. Weng, Y. Shi, H. Lei, Y. Sun, T. Qian, and H. Ding, Observation of unconventional chiral fermions with long Fermi arcs in CoSi, *Nature* **567**, 496 (2019), [arXiv:1901.03358](#).
- [43] D. S. Sanchez, I. Belopolski, T. A. Cochran, X. Xu, J.-X. Yin, G. Chang, W. Xie, K. Manna, V. Süß, C.-Y. Huang, N. Alidoust, D. Multer, S. S. Zhang, N. Shumiya, X. Wang, G.-Q. Wang, T.-R. Chang, C. Felser, S.-Y. Xu, S. Jia, H. Lin, and M. Z. Hasan, Topological chiral crystals with helicoid-arc quantum states, *Nature* **567**, 500 (2019), [arXiv:1812.04466](#).
- [44] T. A. Cochran, I. Belopolski, K. Manna, M. Yahyavi, Y. Liu, D. S. Sanchez, Z.-J. Cheng, X. P. Yang, D. Multer, J.-X. Yin, H. Borrmann, A. Chikina, J. A. Krieger, J. Sánchez-Barriga, P. Le Fèvre, F. Bertran, V. N. Strocov, J. D. Denlinger, T.-R. Chang, S. Jia, C. Felser, H. Lin, G. Chang, and M. Z. Hasan, Visualizing Higher-Fold Topology in Chiral Crystals, *Phys. Rev. Lett.* **130**, 066402 (2023).
- [45] N. B. M. Schröter, D. Pei, M. G. Vergniory, Y. Sun, K. Manna, F. de Juan, Jonas. A. Krieger, V. Süß, M. Schmidt, P. Dudin, B. Bradlyn, T. K. Kim, T. Schmitt, C. Cacho, C. Felser, V. N. Strocov, and Y. Chen, Chiral topological semimetal with multifold band crossings and long Fermi arcs, *Nat. Phys.* **15**, 759 (2019), [arXiv:1812.03310](#).
- [46] C.-T. Chen, U. Bajpai, N. A. Lanzillo, C.-H. Hsu, H. Lin, and G. Liang, Topological Semimetals for Scaled Back-End-Of-Line Interconnect Beyond Cu, in *2020 IEEE Int. Electron Devices Meet. IEDM*, Vol. 2020-Decem (IEEE, 2020) pp. 32.4.1–32.4.4, [arXiv:2103.10505](#).
- [47] N. A. Lanzillo, U. Bajpai, I. Garate, and C.-T. Chen, Size-Dependent Grain-Boundary Scattering in Topological Semimetals, *Phys. Rev. Appl.* **18**, 034053 (2022), [arXiv:2206.08214](#).
- [48] A. C. Potter, I. Kimchi, and A. Vishwanath, Quantum oscillations from surface Fermi arcs in Weyl and Dirac semimetals., *Nat. Commun.* **5**, 5161 (2014), [arXiv:1402.6342](#).
- [49] F. D. M. Haldane, Attachment of Surface "Fermi Arcs" to the Bulk Fermi Surface: "Fermi-Level Plumbing" in Topological Metals, *Prepr. ArXiv14010529*, **5** (2014), [arXiv:1401.0529](#).
- [50] G. Chang, J. Yin, T. Neupert, D. S. Sanchez, I. Belopolski, S. S. Zhang, T. A. Cochran, Z. Chéng, M.-C. Hsu, S.-M. Huang, B. Lian, S.-Y. Xu, H. Lin, and M. Z. Hasan, Unconventional Photocurrents from Surface Fermi Arcs in Topological Chiral Semimetals, *Phys. Rev. Lett.* **124**, 166404 (2020), [arXiv:1906.03207](#).
- [51] I. C. Fulga and A. Stern, Triple point fermions in a minimal symmorphic model, *Phys. Rev. B* **95**, 241116 (2017), [arXiv:1702.03939](#).
- [52] H.-C. Hsu, I. C. Fulga, and J.-S. You, Disorder effects on triple-point fermions, *Phys. Rev. B* **106**, 245118 (2022), [arXiv:2205.12003](#).
- [53] H. B. Nielsen and M. Ninomiya, Absence of neutrinos on a lattice. (I). Proof by homotopy theory, *Nucl. Phys. B* **185**, 20 (1981).
- [54] H. B. Nielsen and M. Ninomiya, Absence of neutrinos on a lattice. (II). Intuitive topological proof, *Nucl. Phys. B* **193**, 173 (1981).
- [55] H. B. Nielsen and M. Ninomiya, A no-go theorem for regularizing chiral fermions, *Phys. Lett. B* **105**, 219 (1981).
- [56] Z. Ni, K. Wang, Y. Zhang, O. Pozo, B. Xu, X. Han, K. Manna, J. Paglione, C. Felser, A. G. Grushin, F. De Juan, E. J. Mele, and L. Wu, Giant topological longitudinal circular photo-galvanic effect in the chiral multifold semimetal CoSi, *Nat Commun* **12**, 154 (2021), [arXiv:2006.09612](#) [[cond-mat.mtrl-sci](#)].
- [57] S. Nandy, S. Manna, D. Călugăru, and B. Roy, Generalized triple-component fermions: Lattice model, Fermi arcs, and anomalous transport, *Phys. Rev. B* **100**, 235201 (2019), [arXiv:1809.04080](#).